

An Adaptive Random Pore Model for Multimodal Pore Structure Evolution with Application to Char Gasification

Simcha L. Singer and Ahmed F. Ghoniem*

Massachusetts Institute of Technology, Department of Mechanical Engineering, Cambridge, Massachusetts 02139, United States

ABSTRACT: An extension of the random pore model has been developed that allows different pore sizes to grow at different rates, depending on the instantaneous pore-scale reactant penetration at a given location within a reacting porous particle. This is accomplished by incorporating pore-scale effectiveness factors, consistent with the random pore geometry, into equations for the growth of each individual pore size. This framework allows the evolution of the char structure with local conversion to adapt to changes in boundary conditions (reactants, temperature) and the development of intraparticle gradients, rather than being predetermined by the initial pore structure (i.e., by the value of the random pore model structural parameter, ψ). This framework also facilitates the calculation of intrinsic kinetic parameters from experimental measurements by providing an estimation of the fraction of the total surface area participating in a given reaction. Without using any fitting parameters, the model has been found to satisfactorily reproduce some coal char oxidation experiments from the literature. The model has also been applied to two cases of practical interest for char particle gasification: zone II reaction conditions and reactants that change over the course of conversion. In these cases, the results of the adaptive random pore model differ from those predicted by the original random pore model.

1. INTRODUCTION

The structural evolution of porous particles undergoing gasification or combustion in the kinetically limited (zone I) or pore diffusion-limited (zone II) regimes is important for predicting burnout behavior, provided intrinsic kinetic expressions are known, and, conversely, for determining proper intrinsic kinetic data from zone I experiments.^{1–4} Many models of pore structure evolution have been developed,^{5–8} with the random pore models (RPMs) being the most ubiquitous, because of their relative simplicity and success in reproducing experimental data obtained under kinetically controlled conditions.

Many porous solids, including coal and biomass char, are known to possess multimodal pore structures.^{9,10} Even in what is ostensibly the kinetically controlled regime, it has been observed that pore sizes below roughly 1–2 nm may not participate in certain char gasification reactions; therefore, the entire initial surface area may not always be the correct initial structural data to be used as input to the pore structure evolution model.^{1,6,11–13}

It was observed by Hurt that CO₂ did not react significantly in the micropores of a sub-bituminous coal char, possibly because of the preferential location of catalyst particles in the larger pores, or the fact that very small pores represent less-reactive regions between basal planes.¹ Other researchers have observed, on several occasions, that O₂ does not react significantly in char micropores with radii below 1–2 nm, and this has been attributed to (i) slow diffusion of O₂ in these small pores,^{10,14} (ii) a reaction mechanism that leads to strong chemisorption of oxygen on micropore surfaces,¹⁵ or (iii) micropores that comprise less reactive sites between basal planes, which can be revealed by the removal of relatively large, obstructing hydrocarbon molecules, but do not participate in oxidation reactions.¹³

Consequently, depending on whether the reactant is oxygen, carbon dioxide, or steam, normalized reaction rate versus conversion curves can exhibit widely differing behavior for the same

char. This is manifested in the observation that, for chars with significant initial microporosity, the normalized rate versus conversion curve may exhibit a distinct maximum when reacted with oxygen, while it may be monotonically decreasing when reacted with carbon dioxide or steam.^{10,15} Other studies on coal chars that apparently contain significant amounts of closed porosity have concluded that O₂ is more effective than CO₂ at opening micropores early in the conversion process, by removing disorganized hydrocarbon molecules leftover from pyrolysis, but that neither gas actually reacts substantially on the surface of the micropores.^{13,16}

To apply a pore structure evolution model when intraparticle species gradients are present, the practice has typically been simply to apply the same structural evolution equations *locally*, while also solving a species conservation equation to account for the fact that the reactant concentration will vary across the porous particle.^{17–20} This implicitly assumes that, at each position in the particle, the entire pore structure evolves in the same manner with local conversion, although this evolution may happen at varying rates, because of the intraparticle species and temperature gradients.

In the pore diffusion regime (zone II), typical of many combustion and entrained flow gasification processes, simulations have indicated that the pore structure evolution has strong effects on the temperature, burnout times, fragmentation, ignition, and extinction behavior of reacting porous char particles.^{18–20} Specifically, when the available internal surface area increases and displays a maximum with conversion, particles burn at higher temperatures, ignite at lower ambient temperatures, experience extinction at higher conversions, and have lower burning times

Received: November 12, 2010

Revised: February 8, 2011

Published: March 11, 2011

than particles with an available internal surface area that decreases monotonically with conversion. Furthermore, under certain conditions, the latter particles exhibited a conversion profile with a maximum inside the particle, while the former always had the maximum local conversion at the particle surface.^{18–20} These particle-scale effects are due to both the influence of the pore surface area on the heterogeneous reaction rates, as well as the influence of the pore structure on the intraparticle diffusion of gaseous species. It should be mentioned that these authors^{18–20} modeled the intraparticle fluxes using the Dusty Gas Model, which employs a single average pore size and has no way of explicitly accounting for a multimodal pore structure.²¹

During entrained flow gasification, coal or biomass char particles with multimodal porous structures are typically subjected to several reactions with widely varying rates, which may occur concurrently or sequentially. Since, in most cases, the reactions occur in the regime of mixed kinetic/intraparticle diffusion control (zone II), the evolving porous structure plays an important role in both the heterogeneous reaction rate and the intraparticle transport. Because of species gradients, temperature gradients, or time-dependent boundary conditions, at certain times and locations within a char particle, the conversion may occur on the surface of the smallest pores, e.g., if $C + H_2O$ is the main reaction at that location and time, while, at other times and locations, the reaction may proceed mostly on the surface of larger pores (e.g., if $C + O_2$ is the main reaction at that position and time). Therefore, the resultant pore structure evolution with local conversion will not be the same throughout the particle and cannot be predicted based solely on the initial structure. This will, in turn, affect the reaction rate and intraparticle gaseous transport and may influence ignition/extinction behavior, temperature, burning times, etc.

The above considerations indicate that, in contrast with the often-invoked assumption, as conversion proceeds and the intraparticle gradients develop, the solid structure does not necessarily evolve in the same manner with local conversion at different *positions* in the porous solid. In addition, because of local species and/or temperature variations, a given location may shift *over time* from reactions occurring on one subset of pores to reactions occurring on a different subset. Furthermore, the assumption of a strict *cutoff* of pore sizes—e.g., 2 nm—that participate in a given heterogeneous reaction may not always be realistic, since this implies that the entire range of pore sizes considered by the structural evolution model (i.e., above the cutoff) are exposed to the local smooth field concentration of reactant, while pores below the cutoff size are assumed not to be penetrated by reactants whatsoever (although they may contribute a constant additional surface area, considered as surface roughness⁶).

In other words, most random pore models designate the pores a priori, as either being in kinetic control (with full reactant penetration) or in complete diffusion control (with no reactant penetration), but a particular pore size cannot be in mixed control and cannot switch from one regime to the other with time or with location. In this work, we use concepts introduced by several researchers^{2,6,22–24} to relax these assumptions and extend the RPM to account for various pore sizes growing at different rates, depending on the local, instantaneous pore-scale reactant penetration throughout the solid particle. This is accomplished by incorporating pore-scale effectiveness factors, consistent with the random pore geometry, into equations for the growth of individual pore sizes.

This extension has important implications for particles reacting in the kinetic regime and for conditions of industrial relevance in which intraparticle gradients are present (zone II) and/or gaseous reactants change over the course of conversion, making it likely that pores of certain sizes will behave differently, according to their location in the particle and with time. Furthermore, under zone II conditions, in addition to affecting the internal surface area (and, thus, the reaction rate), the pore structure evolution also affects the intraparticle fluxes. When the structure is not strictly unimodal, it is most accurate to use a flux model that can explicitly account for this multimodal nature,^{22,25} such as the Feng and Stewart model.²⁶ In such a case, accounting for various pore sizes growing at different rates also can improve the accuracy of the flux model. We will explore this point in more detail in a subsequent paper.

In sections 2.1 and 2.2, we review the original RPM in discrete form and implement a slightly altered version, using equations that allow the evolution of pores of different sizes to be followed separately, which results in a framework with the flexibility necessary to overcome the shortcomings mentioned above. In Section 2.3, we develop a method for quantifying the participation of various pore sizes in any reaction, using pore-scale effectiveness factors, which is consistent with the framework presented in Section 2.2. In Section 2.4, we apply the method of Section 2.3 to normalize measured kinetic data, using the participating surface area, to determine intrinsic (i.e., per unit surface area) kinetic rates. Similar to the original RPM, the current modified version is completely predictive in nature if the necessary initial measurements are performed. In Section 3, validation of the model using data from the literature is performed and examples that illustrate the flexibility of the model in cases of intraparticle gradients and time-dependent boundary conditions are presented.

2. FORMULATION OF THE MODEL

2.1. The Random Pore Model. The random pore model (RPM), developed by Bhatia and Perlmutter⁵ and separately by Gavalas⁶ (who called it the random capillary model), is the basis for predicting the structural evolution of the porous solid and we will follow the development presented by Gavalas.⁶ The RPM was derived under the assumption that the pores consist of straight cylindrical capillaries with axes randomly located and oriented in three-dimensional space, although it can be extended to pores of other shapes.¹³ By simply measuring the initial porosity distribution with pore radius ($\phi(R)$), using porosimetry and gas adsorption experiments, the RPM can be used to predict the pore radii, surface area, and porosity of the reacting porous solid at all subsequent conversions. Because of the assumption of randomly located pores, the density of pore intersections with any plane is a Poisson process with a mean λ , meaning that the number of pores intersecting a spatial area element ds is given by λds . Gavalas also demonstrates that the total length of pore axes per unit volume is given by $l = 2\lambda$, which is constant over time if no new porosity is created or uncovered. Hurt modified the RPM to allow λ to vary over time, as a way of simulating the creation of new pores, in addition to considering pore enlargement due to reaction.²⁷ The method was used to explain the data of Hurt²⁸ and Murrell;²⁹ however, it is not fully predictive, because the ratio of conversion from pore creation to pore widening must be given as an input to the model or adjusted to fit the experimental data.

To have the flexibility to allow various pore sizes to behave differently, we adopt the discrete formulation of the RPM as a starting point.²² When species gradients are present at the particle scale, it may be advantageous to use a discrete form of the RPM to provide consistency with an intraparticle flux model that is appropriate for multimodal porous structures.^{22,25,26} The discrete formulation of the RPM assumes that, at time $t = 0$, there are n discrete pore sizes with radii $R_{0,i}$ and associated porosities $\phi_{0,i}$ which are defined such that the largest pores at $t = 0$ are denoted by (R_m, ϕ_n) at all times, and smaller pores by the subscripts $i = n - 1, n - 2$, etc.

Based on the volume of the cylindrical pores i , the Poisson distribution dictates that the probability that a point in space is not covered by any pore of size i is

$$\begin{aligned} \text{Probability of a point not covered by any pore } i \\ = \exp(-\pi l_{0,i} R_i^2) \end{aligned} \quad (1)$$

where the length of pore axes i per unit volume, including those axes that are overlapped by larger pores, is $l_{0,i} = 2\lambda_i$ (in Bhatia and Perlmutter's derivation and notation, the sum of all $l_{0,i}$ would correspond to $L_{E,0}$, rather than L_0).

A volume that is covered by more than one overlapping pore size is assigned to the largest pore size that overlaps it, which makes physical sense and is consistent with experimental determinations of $\phi(R)$. Based on this definition and the fact that the probabilities of coverage by different pore sizes are independent, it is possible to write equations for the individual porosities corresponding to pores i , ϕ_i , and the total porosity, ϕ_{Tot} :²²

$$\phi_i = [1 - \exp(-\pi l_{0,i} R_i^2)] \exp(-\pi \sum_{j=i+1}^n l_{0,j} R_j^2) \quad (2)$$

$$\phi_{\text{Tot}} = 1 - \exp(-\pi \sum_{j=1}^n l_{0,j} R_j^2) \quad (3)$$

The right-hand side of eq 2 represents the probability that a volume is covered by a pore i (the first term in brackets) and that it is not covered by any pores of size j larger than i (second term). The two probabilities on the righthand side of eq 2 are independent; therefore, their product gives the joint probability of a volume belonging to pores i . Equation 3 for the total porosity simply results upon summing eq 2 over all pore sizes i .

More conveniently, from the standpoint of measurements, it is possible to rearrange eq 2 to determine the total length of pore axes of each size, $l_{0,i}$, using the discrete values of initial porosity ($\phi_{0,i}$) and radius ($R_{0,i}$), which can be obtained experimentally:²²

$$l_{0,i} = \frac{1}{\pi R_{0,i}^2} \ln \left(\frac{1 - \sum_{j=i+1}^n \phi_{0,j}}{1 - \sum_{j=i}^n \phi_{0,j}} \right) \quad (4)$$

To model the changing structure (i.e., the pore radii, total porosity, and pore surface area) of the porous solid as it is consumed, most implementations of the RPM (with some exceptions that will be discussed later^{23,30}) have assumed that all pores considered by the model (either all the pores, or the entire range of pores above a cutoff radius) at a given location increase their radii by the same amount, $q(r,t)$, which depends on the local conversion, $X(r,t)$:

$$R_i(r,t) = R_{0,i}(r) + q(r,t) \quad (5)$$

Based on eqs 3, 5, and by noting that, as the pore radius increases by an amount dq , the volume of the pores per unit volume increases by an amount $d\phi = S dq$, Gavalas obtained an expression relating the pore surface area per unit volume (S) to the pore growth variable (q), by differentiating eq 3 with respect to q (for clarity, from this point, we drop the reference to r and t in the equations):

$$\begin{aligned} S = \frac{\partial \phi_{\text{Tot}}}{\partial q} &= (1 - \phi_{\text{Tot}}) \sum_i 2\pi l_{0,i} (R_{0,i} + q) \\ &= (1 - \phi_{\text{Tot}}) \sum_i 2\pi l_{0,i} R_i \end{aligned} \quad (6a)$$

It can be verified, after some manipulations, that this is exactly equivalent to the equation for surface area evolution derived by Bhatia and Perlmutter:⁵

$$S = S_0(1 - X) \sqrt{1 - \psi \ln(1 - X)} \quad (6b)$$

where S_0 is the initial surface area, and the structural parameter of the RPM (ψ), given in terms of quantities employed in the random capillary model, is

$$\psi = \frac{\sum_i l_{0,i}}{\pi (\sum_i l_{0,i} R_{0,i})^2} \quad (6c)$$

The surface area multiplies the intrinsic heterogeneous reaction rate (\mathcal{R}_k , expressed in units of mol/(m² s)), in the differential equation describing the evolution of the solid conversion with time:

$$\frac{dX}{dt} = \frac{-MW}{\rho_{\text{True}}(1 - \phi_{0,\text{Tot}})} S \sum_k \nu_{C,k} \mathcal{R}_k \quad (7)$$

where MW is the molecular weight of the solid, $\nu_{C,k}$ the stoichiometric coefficient of the solid (char) in reaction k , and ρ_{True} the true solid density. Solid conversion, which varies from zero to unity, is related to the porosity by

$$X = \frac{\phi_{\text{Tot}} - \phi_{0,\text{Tot}}}{\phi_{\text{Final}} - \phi_{0,\text{Tot}}} \quad (8)$$

and, upon substituting for $\phi_{0,\text{Tot}}$ and ϕ_{Tot} in the definition of conversion, and using $\phi_{\text{Final}} = 1$, even with ash present, similar to Lu and Do,³¹ a quadratic equation relating q and X can be derived:

$$(\pi \sum_i l_{0,i}) q^2 + (2\pi \sum_i l_{0,i} R_{0,i}) q + \ln(1 - X) = 0 \quad (9)$$

This closes the set of equations needed to determine the conversion (eq 7), pore radii (eqs 5 and 9), total porosity (eq 3), and pore surface area (eq 6a).

2.2. Adaptive Random Pore Model (ARPM). To address the shortcomings mentioned in the Introduction, we implement, for each pore size, i , its own pore growth variable ($q_i(r,t)$), which is the amount that the radii of pores i have increased at a given location r in the particle, at time t , because of solid consumption:

$$R_i = R_{0,i} + q_i \quad (10)$$

This gives us the flexibility to deal with situations in which the degree of participation of pores i in different heterogeneous reactions varies with position and time, according to reactant

concentration, temperature, conversion, etc. The differential equations that describe the consumption of the porous solid over time will be written in terms of dq_i/dt , since writing the differential equation as dX/dt will not be useful in this formulation, as will be discussed later in this section.

We can determine the individual surface areas of pores i ($S_i(r, t)$), from the increase in total pore volume due to an incremental expansion of pores i (dq_i):

$$S_i = \sum_j \frac{\partial \phi_j}{\partial q_i} = \frac{\partial \phi_{\text{Tot}}}{\partial q_i} = (1 - \phi_{\text{Tot}}) 2\pi l_{0,i} (R_{0,i} + q_i) \quad (11)$$

Finally, although it is not necessary for implementation, to gain insight into the solid conversion process, we also define, for each pore size i , its own conversion variable ($X_{\text{True},i}$). However, using the usual linear relationship between conversion and porosity, analogous to eq 8,

$$X_i = \frac{\phi_i - \phi_{0,i}}{\phi_{\text{Final,Tot}} - \phi_{0,\text{Tot}}} \quad (12)$$

is not meaningful in our case, because it accounts for changes in porosities other than solid–gas reactions on pores i . In fact, using this definition, X_i could even become negative if ϕ_i decreases below $\phi_{0,i}$ because of encroachment by larger pores. Rather, we define $X_{\text{True},i}$ as the solid conversion associated solely with the increases in ϕ_i due to solid–gas reactions on the surface of pores i . However, it is not convenient to use $X_{\text{True},i}$ in the differential equations, because it will be impossible to relate the various $X_{\text{True},i}$ values to the q_i values algebraically, which are needed in the expressions for S_i .

To elaborate on the last point, we note that, although it is possible to use the Poisson distribution to calculate the overlap volume between many different combinations of porosity, correcting for the contributions to $X_{\text{True},i}$ due to overlap cannot be accomplished without knowing the *history* of the pore structure evolution. For example, consider a small volume that is initially in the solid but, at time t , is covered by two different pore sizes. If the larger pore size expanded into the volume after the smaller one, one must correct for the respective porosity gain and loss caused by the overlap, because the overlap caused the porosities to be reclassified. However, if a smaller pore expands into the volume after the larger one, no correction is necessary, since the overlap volume is already included in the larger pore size by definition, which is consistent with eq 2. Thus, knowledge of the *order* of the expansion of all pores is required to make the corrections necessary to relate $X_{\text{True},i}$ to q_i algebraically.

Therefore, we simply use q_i as the state variables²² and write differential equations relating these variables to the solid reaction rates on the walls of pores i , as well as to pore scale effectiveness factors $\eta_{i,k}$, which quantify the participation of each pore size i in each reaction k :

$$\frac{dq_i}{dt} = f\left(\sum_k \mathcal{R}_{k,i} \eta_{i,k}\right) \quad (13)$$

The form of the right-hand side of eq 13 and the pore scale effectiveness factors will be discussed in more detail in section 2.3.

As mentioned previously, both Bhatia²³ and Sotirchos et al.³⁰ have developed models in which each discrete (or discretized) pore size evolves separately and have analogues of eqs 10, 11, and 13. With the goal of modeling the structural evolution in cases where pores may experience plugging (due to solid products possessing greater volume than the solid reactants), those

authors considered situations in which the reaction rate on each pore size is dependent on the reactant concentration reaching the reaction surface after penetrating from the pore surface through a product layer. Thus, reaction rate and pore growth could vary with pore size and location in the particle.

Our work differs from theirs in that we consider the effects of transport limitations caused by the competition between reaction and diffusion throughout the entire random pore structure, whereas Bhatia and Sotirchos^{23,30} consider all pores, regardless of size and interconnectedness, to possess the smooth field value of reactant concentration at the pore surface. The different applications are manifested as different forms of the righthand side of the pore growth evolution equations (eq 13).

Although it is not possible to determine $X_{\text{True},i}$ analytically, the instantaneous change in $X_{\text{True},i}$ is related to the instantaneous increase in q_i by

$$\frac{dX_{\text{True},i}}{dt} = \frac{S_i}{(1 - \phi_{0,\text{Tot}})} \frac{dq_i}{dt} \quad (14)$$

and, therefore, $X_{\text{True},i}(r, t)$ is given by numerically integrating

$$X_{\text{True},i}(q_i) = \frac{1}{1 - \phi_{0,\text{Tot}}} \int_0^{q_i} S_i(q'_i, q_j(q'_i)) dq'_i \quad (15)$$

where q'_i is a dummy variable of integration. S_i depends on the history of q_i and all other q_j . Even though $X_{\text{True},i}$ is not required for implementation of the model, it is useful in analyzing the amount of conversion attributable to reactions on various pore sizes.

To our knowledge, previous RPMs have not utilized separate q_i and S_i values for different pore sizes, together with pore-scale effectiveness factors, to quantify the participation of different pore sizes in different reactions. This extension of the RPM, embodied by eqs 2, 3, 4, 10, 11, and 13, provides a framework with the flexibility necessary to deal with cases when different pore sizes grow at different rates, because of the interplay between transport and kinetics, and allows the pore structure evolution to adapt to instantaneous, local conditions within the solid particle. Equation 13 is now discussed in more detail.

2.3. Pore-Scale Effectiveness Factors. Now that separate expressions for all of the variables associated with the individual pore sizes have been given, it is possible to deal with the fact that, at any location and time, any of the pore sizes may be in a state between complete kinetic and diffusion control for any reaction. We seek to *quantify* the participation of all pore sizes i , at any location, in each reaction k . This information can then be used to describe how the individual pore sizes evolve by writing appropriate ordinary differential equations (ODEs) for the individual pore growth variables, dq_i/dt .

In the appendix of the original random capillary model paper,⁶ Gavalas used the *pore-scale* Thiele modulus (Φ),³² which is a nondimensional number representing the ratio of the reaction rate to the diffusion rate, to determine when pore sizes may be assumed to be in kinetic control, so that the RPM applies to those pores. Typically, a value of $\Phi < 0.3$ is sufficient to assume kinetic control; therefore, Gavalas checked to verify whether this condition was satisfied for all pore sizes considered in his example. For a single cylindrical pore of radius R_p with reaction order n (more-complex kinetic expressions could also be incorporated^{33,34}), the reactant concentration at pore boundary (C_{SF}), intrinsic rate constant ($k_{\text{intrinsic},k}$), stoichiometric coefficient (ν), length (L'_i) (to be discussed later in this section), and an

appropriate diffusion coefficient (D_{eff}) (to be discussed in Section 3), the modulus is given by^{33,35}

$$\Phi_{i,k} = \frac{L'_i}{2} \sqrt{\frac{(n+1)2\nu k_{\text{intrinsic},k} C_{\text{SF}}^{n-1}}{R_i D_{\text{eff}}}} \quad (16)$$

We expand on this idea by calculating, at all times (and locations, if smooth field gradients are present), an overall effectiveness factor, $\eta_{\text{Tot},i,k}$ based on $\Phi_{i,k}$ and the random pore structure, which quantifies the degree of participation of pores i , in reaction k , in a manner that is consistent with the geometry of the ARPM. The effectiveness factor, $\eta_{\text{Tot},i}$ (we now drop reference to reaction k), is then used in conjunction with each individual state equation dq_i/dt to shift smoothly from full to partial to negligible reactant penetration for each pore size i , and to allow the pores to evolve accordingly.

For the simple pore-scale, steady-state, reaction-diffusion equation on which the Thiele modulus Φ is based, it is possible to derive the effectiveness factor η_i , which is defined as the actual rate of conversion in a pore i divided by the theoretical rate if there were no diffusion limitations in the pore. For this situation, the effectiveness factor is given by³⁵

$$\eta_i = \frac{\tanh(\Phi_i)}{\Phi_i} \quad (17)$$

Equations 16 and 17 are exact only for first-order reactions ($n = 1$). For other rate forms, it has been established that the use of the “general modulus” provides a good analytical approximation to the exact solution.³³ For general n th-order rates, the inclusion of the factor $(n+1)/2$ in eq 16 is due to the general modulus (the original Thiele modulus omits this factor).

Equation 17 represents the effectiveness factor for a single pore. However, the porous solid has a distribution of pore lengths for each pore size i (recall that i refers to radius), so the quantity of interest is actually an overall effectiveness factor $\eta_{\text{Tot},i}$ (where the subscript “Tot” indicates that the parameter is a function of the distribution of pore lengths), which is defined as the actual reaction rate for the entire length distribution of pores i , for each reaction, at a given location, divided by the theoretical rate if there were no diffusion limitations in any of those pores. However, as we will see, the fully coupled, nonlinear nature of the final equations for the effectiveness factors will limit our ability to solve for $\eta_{\text{Tot},i}$ while also accounting for the full distribution of lengths, so we will apply a first-order analysis in determining $\eta_{\text{Tot},i}$. In other words, we will simply use the mean pore length, L'_i , in evaluating Φ_i in eq 17 and this will yield a first-order approximation to the mean effectiveness factor, η_i , which we will take as $\eta_{\text{Tot},i}$. Some of the branching pore models, which assume a fractal porous structure with known pore lengths and radii, have employed the concept of calculating a Thiele modulus and effectiveness factor for each level of the assumed hierarchical pore structure.^{14,24} Here, we apply this concept to the evolving geometry of the RPM.

To derive the Thiele modulus given by eq 16, one simply nondimensionalizes a simplified version of a pseudo-steady-state reaction–diffusion equation (neglecting multicomponent diffusion and Stefan flow) for the pertinent geometry, which, in our case, is a single cylindrical pore. One of the parameters required for the Thiele modulus is the characteristic length for pore-scale diffusion, which, in this case, is half the mean length of a pore i . Gavalas’ derivation of the RPM is quite flexible; he derived the expected number of intersections, per unit length of pores i , between pores i and j :⁶

$$n'_{i,j} = \frac{\pi l_{0,j}(R_i + R_j)}{2} \quad (18)$$

The mean length for a pore i is defined as the distance between intersections with any larger pores.⁶ Since the intersections are independent Poisson processes and we seek the distance between intersections with *any* larger pores, we can simply sum the individual $n'_{i,j}$ to get the new rate parameter representing the frequency of intersections with any larger pore size. Then, since the number of intersections with larger pores is still Poisson-distributed, the length between intersections follows an exponential distribution. Therefore, the mean distance between intersections of pores i with larger pores (L'_i) is given by the inverse of the Poisson rate parameter:⁶

$$L'_i = \left(\sum_{j=i+1}^n n'_{i,j} \right)^{-1} \quad (19)$$

The mean length of pores i is a diffusion length scale; it is a distance over which the local smooth field reactant concentration, which serves as the pore-scale boundary condition, may be depleted upon penetrating pore i . Equation 19 implicitly assumes that all of the larger pores intersecting a given pore size i are themselves fully penetrated locally by reactant, such that the concentration in those pores equals the smooth field concentration, C_{SF} , which is used as the boundary condition for pores i . When using a continuum description for transport in the porous particle, $C = C_{\text{SF}}$ within the largest pores, $i = n$, is typically a good assumption,²¹ so full local penetration is assumed for the largest pores and $\eta_{i=n} = 1$. For the next smallest pore size ($i = n-1$), we know that all of the intersections with larger pores have the boundary condition $C = C_{\text{SF}}$. However, for all subsequently smaller pore sizes ($i = n-2, n-3, \dots$, etc.), we must account for the fact that some of the larger pores intersecting pores i may not be in kinetic control, and therefore the boundary condition $C = C_{\text{SF}}$ is not applicable to those intersections. In that case, eq 19 overestimates the number of relevant intersections and underestimates the mean length for diffusion.

For pores i to have boundary condition $C = C_{\text{SF}}$, the larger pores with which they intersect must be fully penetrated by the local smooth field reactant concentration. The effectiveness factor given by eq 17 accounts for species gradients reducing the reaction rate ($\mathcal{R} = k_{\text{intrinsic}} C_{\text{SF}}^n$), as well as the fact that the entire pore surface area may not be accessible, because of the reactant concentration essentially going to zero within the pore.

However, it is possible to idealize the concept by visualizing the effectiveness factor as being due solely to a reduction in accessible surface area within pores i , but with a reactant concentration that remains C_{SF} throughout that exposed area. In accordance with this idealized view of the effectiveness factor, the fraction of the entire length of larger pores, j , with the smooth field boundary condition $C = C_{\text{SF}}$, is now given by η_j . Therefore, when calculating the mean pore length between intersections, we utilize the number of intersections between pores i and larger pores j , which have the local smooth field concentration, instead of the total number of i – j intersections. Since this fraction can be approximated using the effectiveness factor η_j of the larger pores, the following expression should be used in place of eq 19:

$$L'_i = \left(\sum_{j=i+1}^n n'_{i,j} \eta_j \right)^{-1} \quad (20)$$

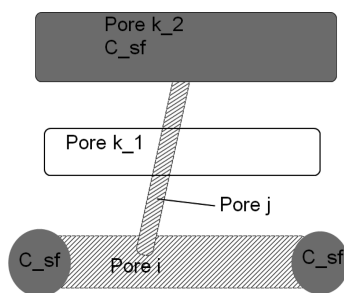


Figure 1. Schematic illustrating the need to consider all $j-i$ intersections but only a fraction, η_k , of $j-k$ intersections when calculating L'_j .

In calculating the Thiele modulus for the interconnected geometry of the ARPM, we must also account for the fact that a given pore has many other smaller pores that intersect it,^{6,24} and, therefore, the surface area for reaction on a pore i is larger than simply $2\pi R_i L'_i$, so eq 16 also must be modified to account for this. The surface area of smaller pores j intersecting a unit length of pore i is given by $2n'_{j,i}\pi R_j L'_j$ and the reaction on the surfaces of pores j may also be subject to diffusion limitations. Therefore, Φ_i depends on η_j for all smaller pore sizes j and is given by

$$\Phi_i = \frac{L'_i}{2} \sqrt{\frac{n+1}{2} \left(\frac{\nu k_{\text{intrinsic}} C_{\text{SF}}^{n-1}}{D_{\text{eff},i}} \right) \left(\frac{2}{R_i} + \sum_{j=1}^{i-1} \frac{2R_j L'_j n'_{j,i} \eta_j}{R_i^2} \right)} \quad (21)$$

in which the summation term accounts for the surface area of smaller pores j that intersect pore i .

The definition of an appropriate mean length (L'_j) for the smaller pores j branching from the pores i also requires consideration. L'_j should be calculated by considering the intersections of pores j with any pores i (regardless of whether pore i has $C = C_{\text{SF}}$) and the intersections between pores j with any other pores k , larger than or equal to i , that have the local smooth field concentration (this fraction being η_k for each $k \geq i$).

We note that, for the purpose of calculating L'_j , we consider all pores i and not just the fraction η_i (as we do with pores k), because we are calculating L'_j to determine the surface area of smaller pores j branching from pores i . This situation is illustrated in Figure 1. The surface area under consideration is the dashed areas of pore i and pore j ; pore k_1 does not have the smooth field concentration, while the pore k_2 does. The area of pores i and j , between the smooth-field boundary conditions shown in gray in Figure 1, is what contributes to the depletion of C_{SF} between the two ends of pore i , so regardless of whether pore i has the smooth field reactant concentration, the $j-i$ intersection must be considered in determining the length of pore j . However, one must only consider intersections of pore j with pores k that have the smooth field reactant concentration, because accounting for the $j-k_1$ intersection will underestimate the surface area branching from pore i that contributes to the depletion of C_{SF} along pore i , since this area actually extends to the $j-k_2$ intersection.

To calculate this mean length, L'_j , we first consider the rate parameter for the Poisson process representing all $j-k$ intersections (where $k \geq i$), $\lambda_{j-k,j-k}$, which is simply

$$\lambda_{j-k,j-k} = \sum_{k=i}^n n'_{j,k} \quad (22)$$

We then *thin* this rate parameter by the probability that, for a given intersection and its closest neighboring intersection, one is a $j-i$ intersection (irrespective of whether pore i has C_{SF}) and the other is any $j-k_{\text{SF}}$ intersection where k has C_{SF} (i.e., k can be any size, larger or equal to i , but it must have C_{SF}). For all of the $j-k$ intersections, each intersection and its nearest neighbor can be either with pore size i or with $k > i$, and can either be among the fraction that has $C = C_{\text{SF}}$ or $C \neq C_{\text{SF}}$. Therefore, we determine the thinning probability by simply summing all 7 of the 16 joint probabilities (which are the products of the marginal probabilities) that fulfill the above criteria, which are shown in Table 1.

After combining terms in the numerator, the thinning probability is given by

$$P_{\text{Thinning}} = \frac{2n'_{j,i} \eta_i - n'^2_{j,i} \eta_i^2 + 2n'_{j,i} \sum_{k=i+1}^n n'_{j,k} \eta_k}{\left(\sum_{k=i}^n n'_{j,k} \right)^2} \quad (23)$$

Therefore, the new rate parameter for determining the frequency of $j-i/j-k_{\text{SF}}$ intersections pairs is

$$\lambda_{j-i,j-k_{\text{SF}}} = \lambda_{j-k,j-k} P_{\text{Thinning}} = \frac{2n'_{j,i} \eta_i - n'^2_{j,i} \eta_i^2 + 2n'_{j,i} \sum_{k=i+1}^n n'_{j,k} \eta_k}{\sum_{k=i}^n n'_{j,k}} \quad (24)$$

and the length between such $j-i$ and $j-k_{\text{SF}}$ intersections is still exponentially distributed with a mean length L'_j , given by the inverse of eq 24:

$$L'_j = \frac{\sum_{k=i}^n n'_{j,k}}{2n'_{j,i} \eta_i - n'^2_{j,i} \eta_i^2 + 2n'_{j,i} \sum_{k=i+1}^n n'_{j,k} \eta_k} \quad (25)$$

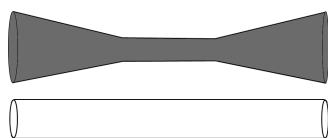
Inserting eqs 20 and 25 into eq 21, the final equation for the modulus for each pore size is given by

$$\Phi_i = \left\{ \left(\frac{n+1}{2} \right) \frac{\nu k_{\text{intrinsic}} C_{\text{SF}}^{n-1}}{4D_{\text{eff},i} \left(\sum_{j=i+1}^n n'_{j,i} \eta_j \right)^2} \left[\frac{2}{R_i} + \frac{2}{R_i^2} \sum_{j=1}^{i-1} \left(\frac{R_j n'_{j,i} \eta_j \sum_{k=i}^n n'_{j,k}}{(2n'_{j,i} \eta_i - n'^2_{j,i} \eta_i^2 + 2n'_{j,i} \sum_{k=i+1}^n n'_{j,k} \eta_k)} \right) \right] \right\}^{1/2} \quad (26)$$

Equations 17 and 26 are applied to determine the effectiveness factor for each pore size, at each location and for each reaction. Although it appears somewhat complex, eq 26 can be implemented for all pore sizes i without too much trouble, using matrix operations. Furthermore, these nonlinear equations should converge quickly, given that the solutions are bounded between zero and unity and that the effectiveness factors do not change too much between time steps. (For this latter reason, during the integration of the q_i in time, it may also be possible to lag the η_i on the right-hand side of eq 26 if the time steps are small enough.) Since each Φ_i and η_i are now coupled to the effectiveness factors

Table 1. Marginal Probabilities for Each $j-k$ Intersection (Column Entries) and Its Nearest Neighbor (Row Entries), and the Combinations That Satisfy the Thinning Criteria

	probability of $j-k$ intersection being:	pore i with C_{SF}	pore i without C_{SF}	pore $k > i$ with C_{SF}	pore $k > i$ without C_{SF}
probability of nearest neighboring $j-k$ intersection being:		$\frac{n_{j,i} \eta_i}{\sum_{k \geq i} n_{j,k}}$	$\frac{n_{j,i} (1 - \eta_i)}{\sum_{k \geq i} n_{j,k}}$	$\frac{\sum_{k > i} n_{j,k} \eta_k}{\sum_{k \geq i} n_{j,k}}$	$\frac{\sum_{k > i} n_{j,k} (1 - \eta_k)}{\sum_{k \geq i} n_{j,k}}$
pore i with C_{SF}	$\frac{n_{j,i} \eta_i}{\sum_{k \geq i} n_{j,k}}$	yes	yes	yes	
pore i without C_{SF}	$\frac{n_{j,i} (1 - \eta_i)}{\sum_{k \geq i} n_{j,k}}$	yes		yes	
pore $k > i$ with C_{SF}	$\frac{\sum_{k > i} n_{j,k} \eta_k}{\sum_{k \geq i} n_{j,k}}$	yes	yes		
pore $k > i$ without C_{SF}	$\frac{\sum_{k > i} n_{j,k} (1 - \eta_k)}{\sum_{k \geq i} n_{j,k}}$				

**Figure 2.** Schematic of the redistribution of the actual uneven conversion (gray pore) to a conversion, which is uniform along the pore axis (white pore).

for all pore sizes, both smaller and larger, we have a system of nonlinear, fully coupled equations. It is for this reason that we have used the mean length between intersections rather than accounting for the entire exponential distribution of lengths.

Other phenomena that occur during char gasification could also be incorporated into this modeling framework. It is possible to modify the model to take into account that there may be a minimum utilization of any pore due to reaction near the pore mouth, even if negligible penetration into the pore occurs,^{14,36} which is similar to the constant roughness provided by the nonreacting micropores discussed by Gavalas.⁶ Other modifications, such as more-complex reaction mechanisms, which account for inhibition and adsorption/desorption phenomena,³⁷ could be taken into account by modifying the pore-scale, generalized Thiele modulus equation. The ARPM framework could also be helpful in capturing the presence of initially inaccessible porosity, since it seems to be a phenomenon associated with certain pore sizes.^{13,16,38}

It should be mentioned that since the ARPM allows situations of partial reactant penetration into the pores, some pores do not react uniformly along their length, distorting their cylindrical shape, which is an assumption that is built into the equations of the RPM. The model essentially redistributes the uneven conversion on a given pore size into a uniform conversion along those pores, shown schematically in Figure 2, thus maintaining cylindrical pores in the ARPM equations. We believe that it is better to take this effect into account using the method outlined above, even though it means that we will be overtly acknowledging the limits of the geometric assumptions of the RPM, which exist in any case. Furthermore, in many cases, the pore-scale effectiveness factors spend much of the conversion near zero or unity, or transition quickly between the two, minimizing the effects of this assumption.

The overall effectiveness factor quantifying the participation of pores i in heterogeneous reaction k at any location is now given by $\eta_{i,k}$. To complete the structural evolution model, at each location, state equations (ODEs) for the pore growth variables due to reactions on each pore size i , by all reactants k , are written:

$$\frac{dq_i}{dt} = \frac{-MW_C}{\rho_{True}} \sum_k \eta_{i,k} \nu_{C,k} \mathcal{R}_k \quad (27)$$

where $\mathcal{R}_k = k_{intrinsic,k} C_{SF,k}^n$ is the heterogeneous reaction rate, and all other variables are as previously defined. Note that pores which are originally not penetrated significantly by reactants ($\eta_i \approx 0$) can eventually begin to react (although q_i and R_i have not increased) due to the decrease in L'_i as larger pores expand and decrease the distance between intersections.

Compared to previous implementations of the RPM, which required a class of pores to be either fully reacting or fully nonreacting, this fraction better represents the actual situation, and instead of dq_i/dt being either zero or its full value, it may assume intermediate values and may change with conversion, which can capture the reality of the interplay between reaction and diffusion at the pore scale, as well as at the particle scale. Essentially, through the η_i , these ODEs become complicated, nonlinear functions of q_i . These n equations (eq 27) for pore growth replace the single equation (eq 7) used in most previous models. When particle-scale gradients are present, these n solid-phase “species equations” can be used in conjunction with any appropriate form of the conservation equations for gaseous species, energy, and momentum in the porous medium. The source terms due to heterogeneous reactions in the equations for gaseous species and energy conservation are proportional to $\mathcal{R}_k \sum_i \eta_{i,k} S_i$ for each reaction k , so eq 11 for the surface areas is utilized explicitly. This formulation allows the quantification of the participation of various pores i in different reactions to vary with position, time, and degree, without any prior assumptions in this regard.

2.4. Method for Determination of Intrinsic Kinetic Rates.

Given the initial porosity distribution $\phi(R)$, the true solid density ρ_{True} , and the inorganic fraction of the reacting solid, the model is fully deterministic if the intrinsic reaction rate is known. However, as mentioned above, in many cases, there is uncertainty associated with intrinsic rate constants, often due to incomplete penetration of reactants into very small pores, even in what is

ostensibly the “purely kinetic” regime. In other words, to determine the intrinsic kinetic rate from conversion measurements, the measured overall reaction rate for the particle must be normalized by the surface area that is participating in the reactions, $\sum \eta_{i,k} S_i$ which is unknown, and is, in fact, an output of the current model.

Sometimes, experimental evidence exists that can be used to determine whether pores of a certain size participate in a particular reaction. As discussed in the Introduction, it has been observed for certain chars reacting with O_2 that the reaction occurs largely within the mesopores (diameters of 2–50 nm) and macropores (diameters of >50 nm), while the micropores (diameters of <2 nm) are mostly inaccessible to oxygen; therefore, the measured rate is best normalized by the mesopore and macropore surface areas.^{11,13,15} However, this type of information is often only qualitative in nature and may be lacking for the purposes of predicting certain intrinsic reaction rates.

Using the equations presented in section 2.3 together with the measured overall conversion rate (dX/dt) and pore structure parameters (S_i , $n'_{i,j}$, etc.) derived from measurements of $\phi(R)$, a quantitative estimate of the surface area that participates in a reaction, and, thus, the intrinsic reaction rate, can be obtained. This assumes that the intrinsic rate is constant with conversion; however, if it is not, the following procedure can be performed more than once, at any point in the conversion that the overall rate and the pore structure data are *both* measured (or known through interpolation). Whenever the overall conversion rate and the pore structure, determined from $\phi_i(R_i)$, are both known, all terms in eqs 17 and 26 are known with the exception of $k_{\text{intrinsic},k}$ which appears in eq 26, and can be written for each reaction k as

$$k_{\text{intrinsic},k} = \frac{k_{\text{Overall, measured},k}}{\sum_i \eta_{i,k} S_i} \quad (28)$$

Now, for each pore size i , eq 28 is substituted into eq 26, which, in turn, is substituted into eq 17, yielding n nonlinear algebraic equations for n unknowns, $\eta_{i,k}$, which can be solved simultaneously. Again, these nonlinear equations should converge quickly, given the fact that the solutions are bounded between zero and unity. Once the individual $\eta_{i,k}$ have been obtained by solving the coupled nonlinear equations above, they can be substituted into eq 28 to determine the intrinsic reaction rate(s).

3. RESULTS AND DISCUSSION

To validate and explore the flexibility of the adaptive random pore model (ARPM), we apply it to the simulation of char gasification. To test the model without using any fitting parameters, data on the complete initial porosity distribution, $\phi(R)$, as well as the true density, ash content, and kinetic parameters (overall rate, activation energy, and reaction order) are required as inputs to the model. Although many studies provide initial surface area and/or porosity values, sometimes even divided into micropore and macropore fractions, ideally, the entire $\phi(R)$ distribution should be used to determine representative discrete radii ($R_{0,i}$) and porosity values ($\phi_{0,i}$) to be used in eq 4.

The data reported by Su and Perlmutter⁹ is one of a few studies^{9,39–41} that have reported the necessary measurements for testing the model. The pore volume distributions that were reported by Su and Perlmutter are the most complete. However, the char consumption experiments of Su and Perlmutter were performed in the kinetic regime (i.e., without any smooth field

species gradients). Therefore, although the data can be used to validate the ARPM, they do not allow the model to exhibit its flexibility in adapting to evolving smooth-field species and temperature gradients or time-dependent boundary conditions.

For chars generated at varying pyrolysis rates and temperatures, Su and Perlmutter performed CO_2 and N_2 adsorption experiments, along with mercury porosimetry, to determine the entire initial pore volume distribution, as a function of pore radius. To test the predictive power of the original RPM, the conversion rate versus conversion curves were measured and the RPM structural parameter ψ determined from the original pore structure was compared to the value of ψ that was determined by fitting the data. The structurally based parameter ψ was determined using the equation given by Bhatia and Perlmutter:⁵

$$\psi = \frac{4\pi L_{0,\text{Tot}}(1 - \phi_{0,\text{Tot}})}{S_{0,\text{Tot}}^2} \quad (29)$$

It can be shown that this expression for ψ is identical to eq 6c, although it should be noted that $L_{0,\text{Tot}} = (1 - \phi_{0,\text{Tot}}) \sum_i L_{i,0}$. When certain pore sizes are assumed to be nonreacting, it can also be shown that eq 6c should only be summed over the reacting pore sizes.

As mentioned by Bhatia and Vartak,⁴² the structure-based ψ should be determined from the initial porosity distribution by assuming that pore overlap exists at $X = 0$, using summations of eqs 4 and 11, or their continuous counterparts integrated over all pore sizes:

$$L_{0,\text{Tot}} = (1 - \phi_{0,\text{Tot}}) \int_0^\infty \frac{\phi(R)}{\pi R^2 [1 - \int_R^\infty \phi(R') dR']} dR \quad (30)$$

$$S_{0,\text{Tot}} = (1 - \phi_{0,\text{Tot}}) \int_0^\infty \frac{2\phi(R)}{R [1 - \int_R^\infty \phi(R') dR']} dR \quad (31)$$

This is in accordance with Gavalas⁶ and in contrast to the procedure originally adopted by Su and Perlmutter and several others, which neglected overlapping porosity at $X = 0$. This has been taken into account in determining ψ in the comparisons presented below.

Oxidation measurements on coal chars were performed by Su and Perlmutter in air at several temperatures, all in the kinetically controlled regime, as determined by the lack of change in reaction rate with varying particle size, as well as the constancy of the activation energy. For application of the ARPM and determination of $k_{\text{intrinsic},k}$ the overall reaction rate at zero conversion is required, since this was the point at which the pore structure was measured. Since the first data point for reaction rate was taken at a conversion of $\sim 10\%$, extrapolation back to $X = 0$ was required. Assuming that the effectiveness factor for each pore size is roughly constant throughout conversion, plotting $(1/(1 - X) \times dX/dt)^2$ vs $-\ln(1 - X)$ should yield a straight line. The overall reaction rate constant $k_{\text{Overall,measured}}$ can then be determined by measuring the intercept at $-\ln(1 - X) = 0$, to which it is proportional. The reaction order (n) was determined experimentally to be unity and the activation energy was also determined experimentally using Arrhenius plots for each sample.⁹ Su and Perlmutter assumed that the entire measured surface area was accessible for reaction at $X = 0$, i.e., $k_{\text{Overall,measured}} = k_{\text{intrinsic}} S_{0,\text{Tot}}$ and used this value in determining $k_{\text{intrinsic},k}$. Rather than assuming that the entire pore surface area is available for reaction, we use the method outlined in section 2.4

Table 2. Parameters Employed in Testing the ARPM with the Experiments of Su and Perlmutter⁹

sample	Temp [K]	ϕ_{micro}	R_{micro} [Å]	ϕ_{meso}	R_{meso} [Å]	ϕ_{macro}	R_{macro} [Å]	E_{O_2} [kJ/mol]	$dX/dt _{X=0}$ [1/s]	ρ_{true} [g/cm ³]
B	728	0.109	7.1	0.031	58.9	0.148	1877	89.96	10.3×10^{-4}	1.42
E	703	0.089	6.7	0.034	105.5	0.137	1918	110.87	7.5×10^{-4}	1.54

to determine the participating surface area and calculate the intrinsic reaction rate constant ($k_{\text{intrinsic}}$). As mentioned by Su and Perlmutter, there is some uncertainty in $k_{\text{Overall,measured}}$, since the plots are not perfectly linear, especially at higher conversions. Following the procedure described above, and assuming that all η_i remain roughly constant through the conversion (which turns out to be true), we recalculated extrapolated values for the initial reactivity based on just the first five data points.

All of the chars from Su and Perlmutter were produced by pyrolyzing coal at very slow heating rates (10 K/min or less), and three of the six chars have initial porosities of <20% (it appears that the porosity given for sample D in their Table 4 is in error). To ensure that the pore structure was well connected⁴³ and a uniform smooth field reactant concentration prevailed throughout the particle, we chose the two highest porosity samples, B and E, for validation of the ARPM. Furthermore, we used the highest temperature runs available for each char, since those conditions would correspond to the maximum pore-scale diffusion limitations, if such limitations were to exist.

Using the initial continuous $dV/d\ln(r)$ distribution given by Su and Perlmutter, which naturally divided the pore sizes into three ranges (although the delineation is not very sharp for sample E), we determined the discrete values of radii and porosity for eq 4. When increasing the number of pore sizes beyond three, whether for the micropores, mesopores, or macropores, we divided that porosity bin into equal parts and determined the mean radii for the new, smaller, pore size bins. After determining $k_{\text{Overall,measured}}$ and using eqs 4 and 11 to determine $S_{0,i}$, we applied eqs 17, 26, and 28 to solve for the initial effectiveness factors and $k_{\text{intrinsic}}$ simultaneously. Table 2 displays some of the relevant parameters used in the validation. In some cases, the discrete porosity values have been further divided, as described above.

In calculating the Thiele modulus and effectiveness factors, both at time zero and throughout the conversion, we accounted for the fact that several studies, including Su and Perlmutter,⁹ have uncovered evidence that oxygen is subject to severe configurational diffusion limitations in char micropores, since transport becomes an activated process when the diffusing molecule is always under the influence of the pore walls. Experiments quantifying this effect for oxygen on coal char are limited, aside from Salatino,¹⁴ who incorporates the effects of configurational diffusion into the Knudsen diffusion term, following the ideas of Satterfield³⁵ and Floess,⁴⁴ and uses the following combined expression:

$$D_{\text{Knudsen/Configuration},i} = \frac{2R_i}{3} \sqrt{\frac{8RT}{\pi MW}} \exp\left(-\frac{\sigma}{R_i}\right) \quad (32)$$

The pore scale effective diffusivity, for each species, location, and pore size, is then approximated as

$$\frac{1}{D_{\text{eff}}} = \frac{1}{D_{\text{continuum}}} + \frac{1}{D_{\text{Kn/Config}}} \quad (33)$$

By incorporating this definition of diffusivity into the pore-scale Thiele modulus and effectiveness factor, we have accounted for the phenomenon of reduced diffusion of O₂ in micropores

from any type of diffusion,^{10,14} as well as the possibility that the reaction mechanism leads to strong chemisorption of oxygen in micropores, since Salatino suggests that the strong chemisorption can be described by the incorporation of a configurational diffusion resistance.¹⁵

The parameter σ in eq 32, which is related to the activation energy for configurational diffusion, has a significant impact on diffusion in the micropores. Salatino estimates a value of $\sigma = 2 \times 10^{-8}$ m for oxygen diffusion in a bituminous coal char at 693 K (which is similar to the temperatures used by Su and Perlmutter), which is relatively high, because of the propensity of oxygen to chemisorb on the surface of the carbon.¹⁴ Instead of using σ as a fitting parameter, we also employ the value given by Salatino, because of the similarity of the experimental conditions. Since experiments determining σ for H₂O and CO₂ on coal char were not found, we have assumed σ for H₂O and CO₂ to be $(5-10) \times 10^{-9}$ m in the results shown later, corresponding to the known smaller configurational limitations of these molecules.^{9,10}

Figure 3a shows the results for sample B at 728 K. The ARPM is compared to the measured data,⁹ and to the original RPM using structural parameters calculated from eq 29, with L_0 and S_0 calculated from eqs 30 and 31. Without doing any parameter fitting, including for the determination of the intrinsic reactivity, the ARPM matches the experimental data well. Using the original RPM with ψ determined using the entire spectrum of pore sizes clearly does not fit the data as well, since diffusion limitations prevent oxygen from penetrating the smallest pores in these samples. In fact, according to the results of the ARPM, the surface area of the smallest pores contributes negligibly to the reaction at $X = 0$. The original RPM with ψ calculated using L_0 and S_0 , based only on the mesopores and macropores, produces a curve that almost coincides with the results of the adaptive model (the discrepancy is due to the discretized pore sizes used in the ARPM), because, in this case, the pore-scale effectiveness factors are essentially zero for the micropores and unity for all other pores and are basically constant with conversion. Figure 3b illustrates the same comparison for sample E at 703 K. Without using any fitting parameters, the ARPM provides a better match to the shape of the data than the original RPM using ψ based on all pore sizes, although, in this case, neither match the data very well. The same observations regarding the two determinations of ψ apply to this sample as well.

Based on these comparisons we can conclude that the pore-scale effectiveness factors in the ARPM correctly account for the observation that oxygen does not penetrate the small pores to a significant extent. Furthermore, the method of section 2.4 provides an internally consistent manner of determining the intrinsic reactivity that when used in conjunction with the ARPM, provides a fully predictive model for solid consumption that matches the data of Su reasonably well, without any fitting parameters.

Figure 4 illustrates the effect of increasing the number of pore size bins considered by the model. For sample B, after five discrete pore sizes are used, there is only a small change in the

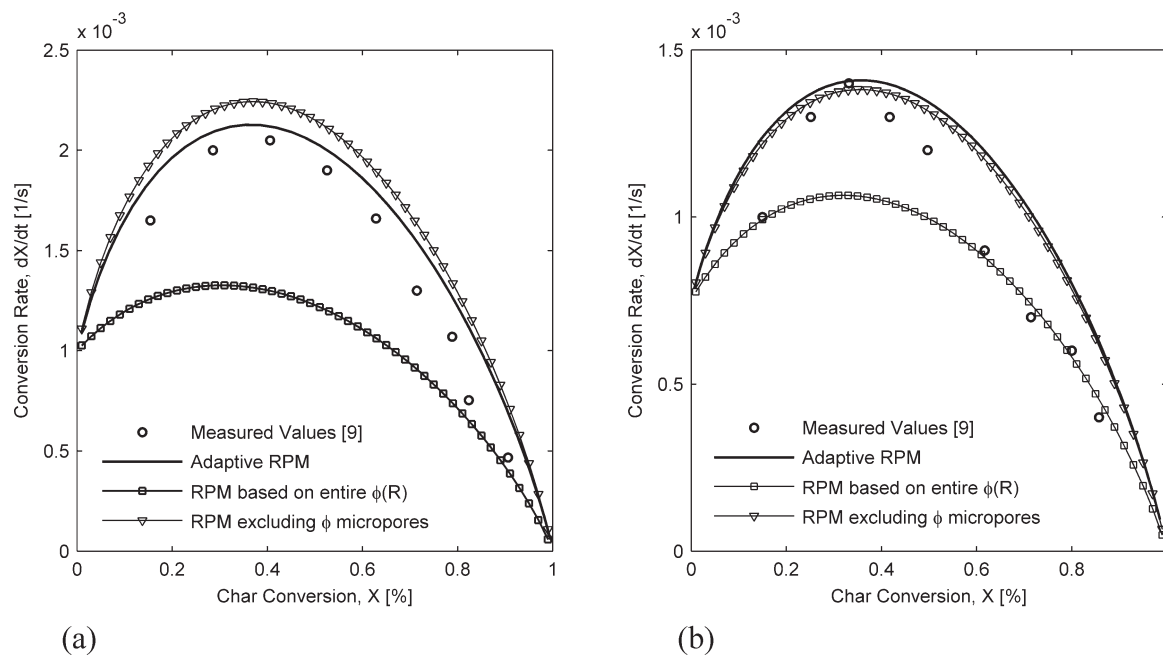


Figure 3. Rate versus conversion using the ARPM with five pore size bins, the RPM based on the entire pore size distribution, the RPM using the pore size distribution excluding micropores and experimental values,⁹ for (a) char sample B in air at 728 K and (b) char sample E in air at 703 K.

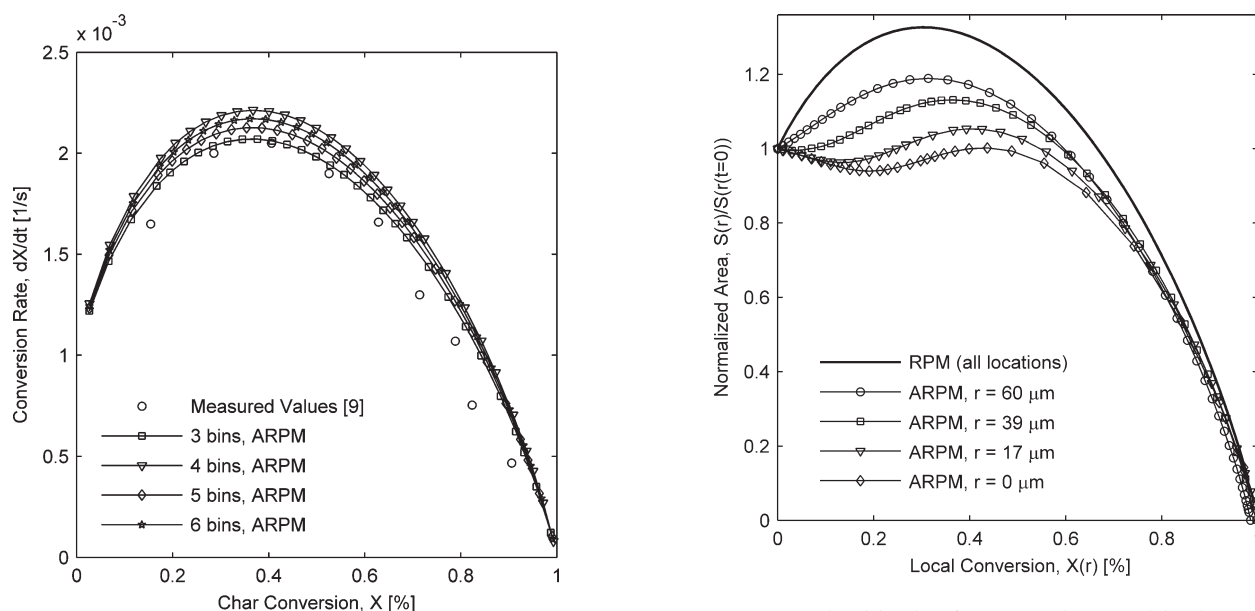


Figure 4. Rate versus conversion using the ARPM with different numbers of pore size bins, compared to the experimentally measured values⁹ for char sample B in air at 728 K.

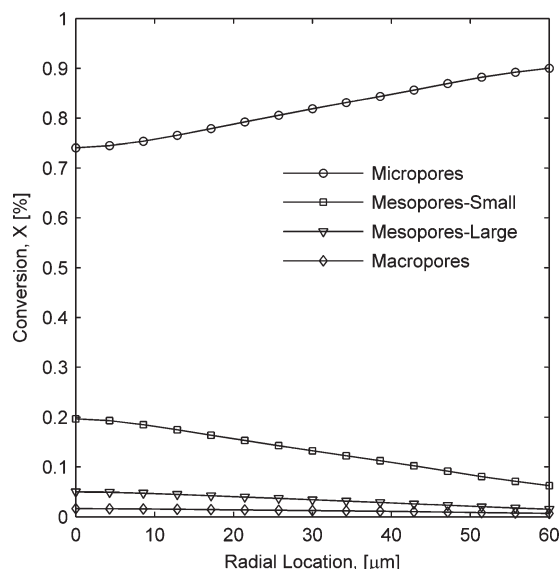
Figure 5. Normalized, local surface area evolution with local conversion for different radial locations in a 128- μm -diameter spherical particle with the properties of char sample B,⁹ in an environment of 10% H_2O , 40% CO_2 , and 50% N_2 at 2000 K and 1 atm.

results, upon increasing the number of pore sizes further. However, note that the best method for determining the discrete pore sizes and radii used in eq 4 may vary with the particular sample and conditions. For example, for this char reacting with oxygen, the subdivision of the micropores into smaller bins has a minimal effect, since the micropores are not penetrated by oxygen to a significant extent, whereas subdividing the mesopores into two or three bins has a larger effect, since they provide the main surface for reaction with oxygen in this case.

As mentioned above, the experiments of Su were done in the kinetically controlled regime, which, in this case, implies only *smooth field* kinetic control, since there are significant diffusion limitations in the micropores. The ARPM predicts values of η_i near unity for all pores above micropore size, and near zero for the micropores, although it changes slightly as conversion proceeds. Nonetheless, the ARPM is capable of handling more-complex situations and can predict $\eta_{i,k}(r,t)$ for conditions when variations in pore utilization exist with pore size i , reactant k , and location r , and vary substantially as conversion proceeds, because

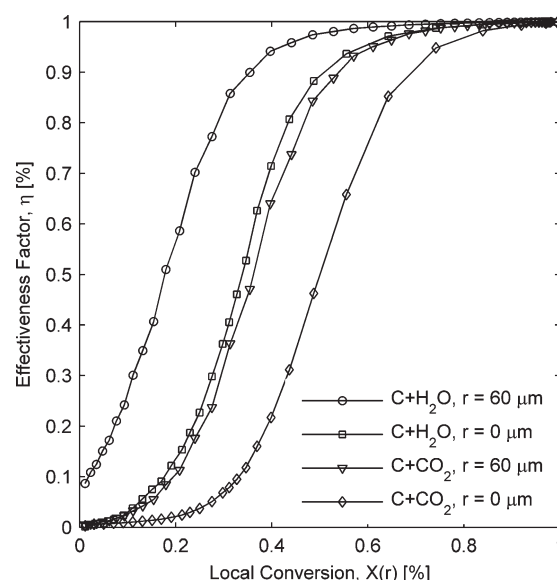
Table 3. Kinetic Parameters Used for Gasification Reactions^a

reaction	$[g/(m^2 s atm^n)]$	E [kJ/mol]	n
$C + CO_2$	202 000	243.2	0.4
$C + H_2O$	226 000	238.2	0.4

^a Data taken from ref 46.**Figure 6.** Final true conversion profiles for char B⁹ in 10% H₂O, 40% CO₂, and 50% N₂ at 2000 K and 1 atm.

of the evolution of smooth field species and temperature gradients. To demonstrate this, the ARPM has been integrated into a simulation of a reacting, spherical, porous particle and its surroundings, consisting of partial differential equations for each gas species, overall mass conservation, energy conservation, and radial momentum conservation, which will be described in a subsequent paper.

Figure 5 illustrates the ability of the model to allow the porous structure at different locations in the particle to evolve in different manners. This figure was obtained by simulating the gasification of a 128- μ m-diameter particle with the properties of char B from Su and Perlmutter, using four pore size bins, in a reducing atmosphere of 10% H₂O, 40% CO₂, and 50% N₂ at a temperature of 2000 K. The intrinsic kinetic parameters employed for these two reactions are shown in Table 3. To illustrate the ARPM's ability to handle variations in pore utilization with pore size, location, and reaction, we have chosen simple n th-order expressions for the gasification reactions. Although char gasification reactions may be better represented by Langmuir–Hinshelwood kinetics in many cases, because of the adsorption–desorption nature of surface reactions and the ability of reaction products to inhibit heterogeneous reactions,^{37,45} our goal here is simply to illustrate the capability of the ARPM; for this reason, we have chosen n th-order rate forms. Using the generalized Thiele modulus,³³ one could incorporate Langmuir kinetics (i.e., without product inhibition) analytically into the ARPM. Computing analytical expressions for the effectiveness factors for Langmuir–Hinshelwood kinetics (with product inhibition) is not possible, although it may be possible to employ the numerical method of Roberts and Satterfield for this purpose.³⁴ For both of these

**Figure 7.** Evolution of micropore effectiveness factors with local conversion for both reactions, for char sample B⁹ in an environment of 10% H₂O, 40% CO₂, and 50% N₂ at 2000 K and 1 atm.

cases, the methods described above for determining the required pore-scale lengths, consistent with the RPM geometry (eqs 20 and 25), would still be applicable.

Despite the fact that the initial pore structure is identical throughout the particle, Figure 5 shows that the surface area evolves differently with local conversion at different locations. Near the outer edge of the particle ($r = 60 \mu\text{m}$), the surface area first increases and exhibits a peak at roughly 34% local conversion. Further toward the particle center, the surface area is either flat or actually decreases with local conversion before beginning to rise and peaking, with the maximum occurring at larger values of local conversion at locations closer to the particle center. Plotting the normalized surface area (rather than the normalized reaction rate, which is affected by the particle-scale species and temperature gradients) shows that the often-used assumption that the structure evolves in the same manner with local conversion may not always be correct. Furthermore, the restriction on the conversion at which the surface area is maximized that is imposed by the RPM ($X_{\text{max}} < 0.393$)^{5,6} is not applicable when the assumptions inherent in the RPM are relaxed, as they are here.

For the same case, examining the final true conversion profiles in Figure 6, which are calculated using eq 15, provides insight into the phenomenon exhibited in Figure 5. Toward the char surface, the particle experiences more conversion on the micropores and less conversion on the larger pores, compared to locations further toward the particle center. Since Figure 5 normalizes the surface area by the total initial surface area, inner locations where the smallest pores participate less in the reaction have smaller normalized areas as conversion proceeds, because the smallest pores experience mostly overlap with larger pores and less growth, until later conversions. At locations closer to the particle surface, the smallest pores experience a greater degree of growth before overlap begins to dominate. The ability of the ARPM to capture an initially uniform pore structure evolving differently, depending on its location, stems from the fact that the model separates the local conversion variable q into separate entities (q_i) and then calculates a separate $\eta_{i,k}(r,t)$ for each one.

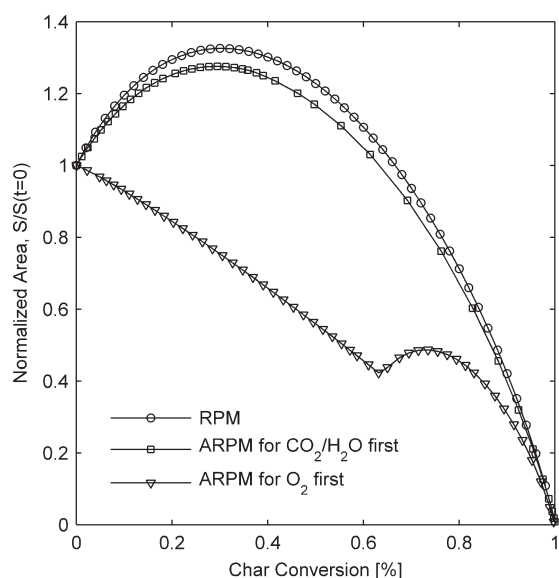


Figure 8. Evolution of normalized surface area with conversion for char sample B⁹ reacting in kinetic control, when exposed first to a gasifying atmosphere, followed by an oxidizing one, and vice versa, according to the RPM (for which there is no difference) and the ARPM.

There are two possible reasons why the micropores participate in the conversion near the particle edge more so than at the center. Under these conditions, intraparticle species gradients exist for both reactants (regime II); however, of the two gasification reactions, under these conditions and with the kinetic expressions employed, the char-steam reaction is roughly 50% faster than the reaction of char with CO₂ and there is less H₂O in the system, leading to steeper gradients of H₂O. Therefore, the C + H₂O reaction dominates near the edge of the particle (at least initially) and the C + CO₂ reaction dominates toward the center of the particle. Furthermore, for the sake of elucidation, we have taken the value of $\sigma_{\text{CO}_2} = 2\sigma_{\text{H}_2\text{O}}$, which is plausible, given the reported ability of H₂O to penetrate very small micropores⁴⁷ and the faster configurational diffusion of H₂O in carbon micropores, compared to CO₂.^{48,49} This means that CO₂ is more diffusion-limited in the smallest pores than H₂O. Therefore, due to the depletion of H₂O across the particle, near the edge, the smallest pores participate in the reaction more than toward the center of the particle, leading to the conversion profiles observed in Figure 6. Second, since, for both reactions, we have employed a fractional reaction order, as reactant concentrations are depleted toward the particle center, the Thiele modulus increases and the effectiveness factor decreases. The micropores effectiveness factors are more sensitive to this than those of the larger pores and thus there is less conversion on the micropores near the particle center.

For this same case, Figure 7 depicts the evolution of the micropore effectiveness factors $\eta_{i=1,k}(r,t)$, with local conversion, for the C + H₂O and C + CO₂ reactions at two different locations (center, $r = 0 \mu\text{m}$ and edge, $r = 60 \mu\text{m}$). Over the course of conversion, all effectiveness factors increase as the pore lengths L'_i decrease and the pore radii increase. It is observed that, throughout conversion, the micropore effectiveness factor is larger for the C + H₂O reaction than for the C + CO₂, at both locations.

More interestingly, even for the C + CO₂ reaction, throughout the conversion, the micropore effectiveness factor is larger for

the edge location ($r = 60 \mu\text{m}$) than for the center location ($r = 0 \mu\text{m}$). This could be explained by the presence of intraparticle species gradients reducing the effectiveness factor toward the particle center for the C + CO₂ reaction, as mentioned above. However, this could also be due to the fact that, near the edge, steam penetrates the smallest pores and reacts, which increases the size of these pores and, thus, also increases the effectiveness factor for the C + CO₂ reaction. In other words, steam activates the micropores near the surface to a greater degree. This explanation is substantiated by Figure 10 (shown later in this paper).

Another situation of practical interest is when the reactant gas to which the particle is exposed changes over the course of conversion. Figure 8 depicts the evolution of the ratio of char surface area to the original surface area with overall conversion for a particle subjected to boundary conditions that change with time. Specifically, the same particle considered above (char B, five pore size bins) is either exposed to an oxidizing atmosphere, followed by a reducing atmosphere, or a reducing atmosphere, followed by an oxidizing one. Unlike Figures 5–7, both conditions correspond to reactions occurring under smooth field kinetic control, although pore-level limitations exist for the oxygen atmosphere, as has been mentioned above. In both cases, the char–O₂ reaction accounts for 64% of the conversion and the char–CO₂ and char–H₂O reactions account for 36% of the conversion. Figure 8 compares the surface area ratio predicted by the ARPM for both situations, as well as predictions of the original RPM, with ψ based on the entire pore size distribution.

When the particle reacts first with oxygen, Figure 8 shows that $S(t)_{\text{Total}}/S_{0,\text{Total}}$ originally decreases, since oxygen cannot penetrate the smallest pores to a significant degree. Therefore, these pores do not experience growth; rather, they only coalesce with larger pores. This decrease in normalized total surface area should not be confused as being contradictory with the observed maximum in the normalized reaction rate when using O₂ as a reactant, as reported by others,^{10,15} since we have already seen in Figures 3 and 4 that the reaction rate of sample B exhibits a distinct peak when reacting under these same oxidizing conditions. In fact, when plotting the normalized reaction rate, the oxidizing conditions show a larger peak than the reducing conditions, which is consistent with experiments.^{10,15}

Rather, as shown in Figure 9a, since the micropores contribute the majority of the surface area, the normalized total surface area ($S(t)_{\text{Total}}/S_{0,\text{Total}}$) closely follows the micropore surface area evolution, which is decreasing, because of the effect of overlap when exposed first to oxygen. When the particle reacts first with CO₂ and H₂O, the normalized surface area increases with conversion and shows a peak before decreasing, as shown in Figure 9b. This is due to the participation of the micropores in the reactions to a greater extent. It can be verified that the evolution of $S(t)_{\text{Total}}/S_{0,\text{Total}}$ and $(dX/dt)/(dX/dt)_0$ coincide only when there are negligible diffusion limitations in all pore sizes (i.e., all $\eta_{i,k}(t) = 1$).

Note that, when the char particle reacts first with CO₂ and H₂O, the subsequent reaction with O₂ *does* occur on the micropores as well. Figures 10a and 10b show the conversion–time behavior for each pore size corresponding to the cases of Figures 9a and 9b, respectively. In Figure 10b, oxygen is slowly added to the system as a boundary condition, beginning at $t = 720 \text{ s}$, and even after the switchover to oxygen is completed, the majority of the char conversion is still due to oxidation reactions that are occurring on the micropores. The reason is

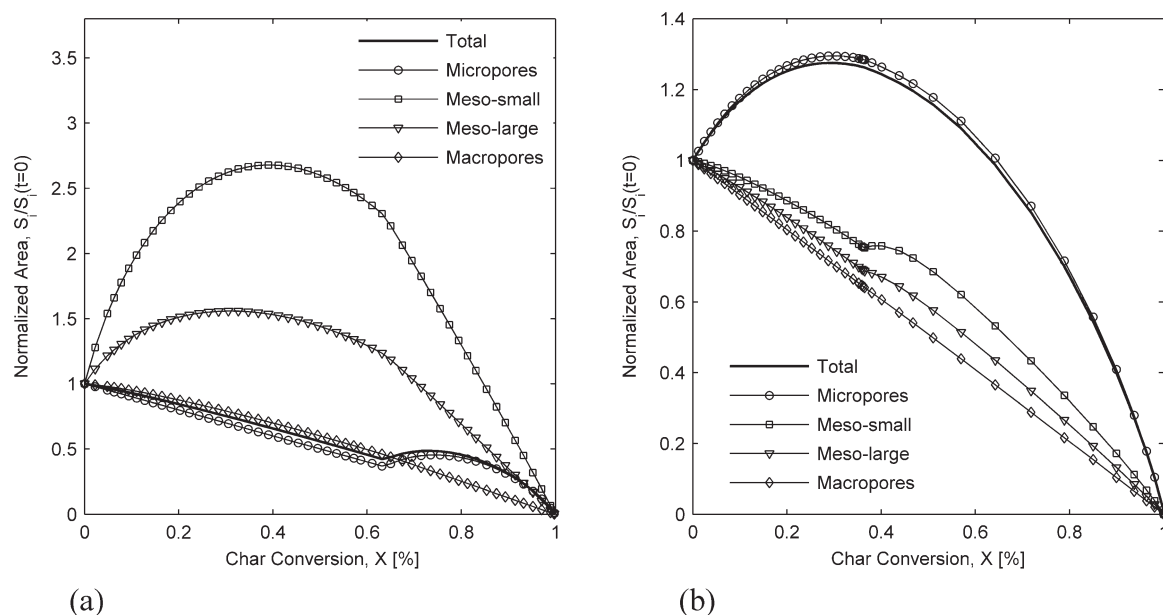


Figure 9. Evolution of normalized total and individual surface areas, S_i , with conversion for char sample B⁹ reacting under kinetic control, predicted by the ARPM, (a) when exposed first to the oxidizing atmosphere and (b) when exposed first to the gasifying atmosphere.

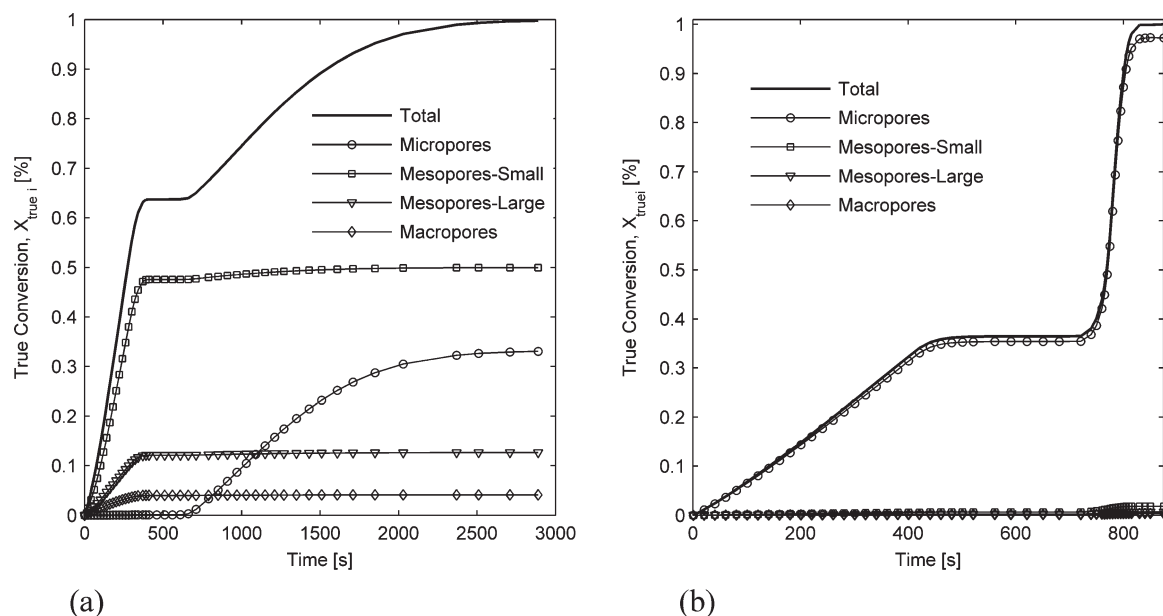


Figure 10. Evolution of X and $X_{True,i}$ on each pore size (a) when exposed first to the oxidizing atmosphere and (b) when exposed first to the gasifying atmosphere.

that, during the initial reaction of the char with CO_2 and H_2O , the micropores expand and subsequently allow for increased penetration of O_2 . In contrast, during the first 600 s of Figure 10a (when oxidation is occurring), a negligible fraction of the conversion occurs on the micropores, since they have not been “activated” first with CO_2 and H_2O .

4. CONCLUSIONS

An extension of the random pore model (RPM) has been developed that allows any pore size, at any location and time, to

be in any state between complete kinetic and diffusion control for any reaction. This has been accomplished by considering, for each pore size, separate equations for pore growth, conversion, and surface area, $(q_{i,j}, X_{True,i,j}, \text{ and } S_i)$, using the random capillary model formulation and by employing pore-scale effectiveness factors, $\eta_{i,j}$ to quantify the participation of all pore sizes in all reactions, at all locations and times. At any time when measured reaction rate and structural data are available, the method can also be applied to determine intrinsic (per unit surface area) kinetic parameters. This framework allows the evolution of the char structure with local conversion to adapt to changes in

boundary conditions or the development of intraparticle species or temperature gradients, rather than being predetermined by the value of the structural parameter, ψ . Without any fitting parameters, the ARPM has been validated with the coal char oxidation data of Su and Perlmutter⁹ with satisfactory agreement, and examples of the flexibility of the model have been provided. Furthermore, the inherent ability of the model to separately quantify the participation of pores of different sizes in different reactions makes it amenable to extensions that account for more-complex phenomena. For example, the opening of initially closed porosity by a particular reactant^{13,16} or the existence of a different initial reactivity⁵⁰ may be phenomena that are associated with certain pore sizes and reactants.

AUTHOR INFORMATION

Corresponding Author

*Tel.: 1-617-253-2295. Fax: 1-617-253-5981. E-mail: gho-niem@mit.edu.

ACKNOWLEDGMENT

This research is funded by the BP-MIT Conversion Research Program.

NOMENCLATURE AND UNITS

A = pre-exponential factor [$\text{mol}/(\text{m}^2 \text{C s } (\text{mol}/\text{m}^3)^n)$] or [$\text{g}/(\text{m}^2 \text{ s atm}^n)$] in Table 3
 C = concentration [mol/m^3]
 D = diffusion coefficient [m^2/s]
 E = activation energy [J/mol]
 $k_{\text{intrinsic}}$ = intrinsic reaction rate constant [$\text{mol}/(\text{m}^2 \text{C s } (\text{mol}/\text{m}^3)^n)$]
 $k_{\text{Overall,measured}}$ = apparent reaction rate constant [$\text{mol}/(\text{m}^3 \text{ s } (\text{mol}/\text{m}^3)^n)$]
 l = total length of pores per unit volume [m/m^3]
 $l_{0,i}$ = total length of pores i per unit volume [m/m^3]
 L'_i = mean distance between intersections of pores i and larger pores [m]
 L'_j = mean length between intersections of pores j with any pores i and with pores k , larger than or equal to i , with the smooth field concentration [m]
 MW = molecular weight [kg/mol]
 n = number of pore bins, or reaction order
 n'_{ij} = expected number of intersections between pores i and j per unit length of pores i [$1/\text{m}$]
 P_{Thinning} = probability that, for a given intersection and its closest neighbor, one is a $j-i$ intersection and the other is any $j-k_{\text{SF}}$ intersection
 q = pore growth variable (uniform) [m]
 q_i = pore growth variable (individual) [m]
 r = radial position within particle [m]
 R = pore radius [m]
 \mathcal{R} = heterogeneous reaction rate [$\text{mol}/(\text{m}^2 \text{C s})$]
 R = gas constant [$\text{J}/(\text{mol K})$]
 S = total pore surface area [$\text{m}^2 \text{C}/\text{m}^3$]
 S_i = pore i surface area [$\text{m}^2 \text{C}/\text{m}^3$]
 t = time [s]
 T = temperature [K]
 V = pore volume (units of ref 9) [cm^3/g]

X = total solid conversion

$X_{\text{True},i}$ = solid conversion due to reaction on pores i

Greek Symbols

ϕ_i = porosity [$\text{m}^3_{\text{pore } i}/\text{m}^3$]
 ϕ_{Tot} = total porosity [$\text{m}^3_{\text{pore}}/\text{m}^3$]
 $\phi(R)$ = porosity distribution with pore radius (units of ref 9) [$\text{m}^3_{\text{pore}}/(\text{m}^3 \text{ Å})$]
 $\eta_{i,k}$ = effectiveness factor for pore i of mean length L'_i in reaction k
 $\eta_{\text{Tot},i,k}$ = effectiveness factor for entire length distribution of pores i in reaction k
 λ = Poisson density [$1/\text{m}^2$]
 ν = stoichiometric coefficient [mol/mol]
 ρ_{True} = true solid density (helium density) [kg/m^3]
 σ = pore radius at which configurational diffusion becomes significant [m]
 ψ = Random Pore model structural parameter
 Φ = Thiele or "general" modulus

Subscripts

0 = at initial time $t = 0$ or initial conversion $X = 0$
 C = char
 continuum = molecular diffusion coefficient
 E = hypothetical property of porous structure without pore overlap
 eff = effective (diffusion coefficient)
 Final = at final time, at $X = 1$
 i = pore size
 j = pore size
 k = pore size, or reaction index
 Kn/Config = combined Knudsen and configurational
 SF = smooth field
 Tot = for the entire distribution of pore lengths
 True,i = due to reaction on pores i

REFERENCES

- (1) Hurt, R. H.; Sarofim, A. F.; Longwell, J. P. *Fuel* **1991**, 70, 1079–1082.
- (2) Hurt, R. H.; Sarofim, A. F.; Longwell, J. P. *Energy Fuels* **1991**, 5, 290–299.
- (3) Roberts, D. G.; Harris, D. J. *Energy Fuels* **2000**, 483–489.
- (4) Campbell, P. A.; Mitchell, R. E.; Ma, L. *Proc. Combust. Inst.* **2002**, 29, 519–526.
- (5) Bhatia, S. K.; Perlmutter, D. D. *AIChE J.* **1980**, 26, 379–386.
- (6) Gavalas, G. R. *AIChE J.* **1980**, 26, 577–585.
- (7) Ballal, G.; Zygourakis, K. *Ind. Eng. Chem. Res.* **1987**, 26, 911–921.
- (8) Yu, H.-chung; Sotirchos, S. V. *AIChE J.* **1987**, 33, 382–393.
- (9) Su, J. L.; Perlmutter, D. D. *AIChE J.* **1985**, 31, 973–981.
- (10) Ballal, G.; Zygourakis, K. *Ind. Eng. Chem. Res.* **1987**, 26, 1787–1796.
- (11) Aarna, I.; Suuberg, E. M. *Twenty-Seventh Symposium (International) on Combustion* **1998**, 2933–2939.
- (12) Radovic, L. R.; Walker, P. L.; Jenkins, R. G. *Fuel* **1983**, 62, 849–856.
- (13) Feng, B.; Bhatia, S. K. *Carbon* **2003**, 41, 507–523.
- (14) Salatino, P.; Zimbardi, F. *Carbon* **1994**, 32, 51–59.
- (15) Salatino, P.; Senneca, O.; Masi, S. *Carbon* **1998**, 36, 443–452.
- (16) Kulaots, I.; Hsu, A.; Suuberg, E. M. *Proc. Combust. Inst.* **2007**, 31, 1897–1903.
- (17) Bhatia, S. K.; Perlmutter, D. D. *AIChE J.* **1981**, 27, 247–254.
- (18) Sotirchos, S. V.; Amundson, N. R. *AIChE J.* **1984**, 30, 537–549.
- (19) Sotirchos, S. V.; Amundson, N. R. *AIChE J.* **1984**, 30, 549–556.
- (20) Morell, J. I.; Amundson, N. R.; Park, S. K. *Chem. Eng. Sci.* **1990**, 45, 387–401.

- (21) Jackson, R. *Transport in Porous Catalysts*; Elsevier: New York, 1977.
- (22) Gavalas, G. R. *Combust. Sci. Technol.* **1981**, *24*, 197–210.
- (23) Bhatia, K. *AIChE J.* **1985**, *31*, 642–648.
- (24) Sheintuch, M.; Brandon, S. *Chem. Eng. Sci.* **1989**, *44*, 69–79.
- (25) Sotirchos, S. V.; Burganos, V. N. *Chem. Eng. Sci.* **1986**, *41*, 1599–1609.
- (26) Feng, C.; Stewart, W. E. *Ind. Eng. Chem. Res.* **1973**, *12*, 143–147.
- (27) Hurt, R. H.; Sarofim, A. F.; Longwell, J. P. *Energy Fuels* **1991**, *5*, 463–468.
- (28) Hurt, R. H.; Dudek, D. R.; Longwell, J. P.; Sarofim, A. F. *Carbon* **1988**, *26*, 433–449.
- (29) Murrell, L. L.; Ratcliffe, C. T.; Pieters, W. J. M.; Sherman, L. G.; Dispenziere, N. C.; Venero, A. F. *Carbon* **1988**, *26*, 33–39.
- (30) Sotirchos, S. V.; Zarkanitis, S. *Chem. Eng. Sci.* **1993**, *48*, 1487–1502.
- (31) Lu, G. Q.; DO, D. D. *Carbon* **1994**, *32*, 247–263.
- (32) Thiele, E. W. *Ind. Eng. Chem.* **1939**, *31*, 916–920.
- (33) Bischoff, K. B. *AIChE J.* **1965**, *11*, 351–355.
- (34) Roberts, G. W.; Satterfield, C. N. *Ind. Eng. Chem. Fundam.* **1965**, *4*, 288–293.
- (35) Satterfield, C. N. *Mass Transfer in Heterogeneous Catalysis*, 1st ed.; M.I.T. Press: Cambridge, MA, 1970; pp 135–136.
- (36) Verhoff, F. H.; Strieder, W. *Chem. Eng. Sci.* **1971**, *26*, 245–253.
- (37) Roberts, D. G.; Harris, D. J. *Fuel* **2007**, *86*, 2672–2678.
- (38) Morimoto, T.; Ochiai, T.; Wasaka, S.; Oda, H. *Energy Fuels* **2006**, *20*, 353–358.
- (39) Salatino, P.; Zimbardi, F.; Masi, S. *Carbon* **1993**, *31*, 501–508.
- (40) Sahu, R.; Levendis, Y. A.; Flagan, R. C.; Gavalas, G. R. *Fuel* **1988**, *67*, 275–283.
- (41) Loewenberg, M.; Levendis, Y. A. *Combust. Flame* **1991**, *84*, 47–65.
- (42) Bhatia, S. K.; Vartak, B. J. *Carbon* **1996**, *34*, 1383–1391.
- (43) Sahimi, M.; Gavalas, G. R.; Tsotsis, T. T. *Chem. Eng. Sci.* **1990**, *45*, 1443–1502.
- (44) Floess, J. K.; VanLishout, Y. *Carbon* **1992**, *30*, 967–973.
- (45) Roberts, D. G.; Harris, D. J. *Energy Fuels* **2006**, *20*, 2314–2320.
- (46) Hla, S. S.; Harris, D.; Roberts, D. *Gasification Conversion Model-PEFR*; Research Report 80; 2007.
- (47) Chi, W.-kuang; Perlmutter, D. D. *AIChE J.* **1989**, *35*, 1791–1802.
- (48) Koresh, J.; Soffer, A. *J. Chem. Soc., Faraday Trans. 1* **1980**, *76*, 2457–2471.
- (49) Walker, P. L. *Carbon* **1996**, *34*, 1297–1299.
- (50) Gupta, J. S.; Bhatia, S. K. *Carbon* **2000**, *38*, 47–58.